

# Inspection of Defects on Whole Ball Surface by View-to-View Mapping Using Zernike Moments

Ku-Chin Lin\* and Min-Hsiung Ma \*\*

**Keywords** : defect inspection, template matching, Zernike moments.

## ABSTRACT

This study develops a novel approach for surface defect inspection of golfball using a view-to-view mapping based on a reduced set of Zernike moments. According to 1,000 random test views conducted in this study, the cycle time of inspection is about 2.0 seconds, which is very competitive to a commercialized deep learning system. With a proposed fine-tuning mechanism, the false alarm rate achieved is 0.6%. To our best knowledge, no such comparable data are available in literature. The proposed inspection algorithm equipped with a non-logo detector using color thresholding works under uneven illumination. It is capable to detect simultaneously logo-attached and non-logo assembly defects of different shapes, sizes, and colors in a single view and resolution. The principle of the proposed view-to-view mapping is applicable for inspection of defects on a wide and highly-curved/plane surface where precise feature alignment for template matching is impractical to perform on line.

## INTRODUCTION

Automatic optical inspection (AOI) techniques have been widely applied for quality control of many industrial products. However, the technique developed for one application is rarely directly applicable for another. The applications may have their own specific clamping mechanism, region of interest (ROI), illumination design, and/or alignment scheme for a wide inspection area. Indeed, advanced techniques are still required, especially for the applications: (1) defects randomly spread over a wide and highly curved or ball surface where precise ROI alignment and uniform illumination design is difficult (2) defects vary simultaneously in shape, size, and color.

*Paper Received December, 2021. Revised January, 2023. Accepted January, 2023. Author for Correspondence: Ku-Chin Lin.*

*\* Professor, Department of Mechanical Engineering, Kun Shan University Tainan, Taiwan, 71070, R.O.C.*

*\*\* PhD Student, Department of Mechanical Engineering, Kun Shan University Tainan, Taiwan, 71070, R.O.C.*

Rosati et al. (2009) designed a defect detection system for an automotive plastic component with curved surfaces coated with high reflective material. They designed a set of mirrors to illuminate the defects of various shapes and dimensions on coating. The defects are detected as shadows against a high brightness background with good uniformity of intensity. Qiang et al. (2015) studied defects of printed circuit boards (PCB) where image stitching is applied to form a whole PCB image for inspection. They extract characteristic lines from views as registration for alignment. Surf registration is used to improve the stitching accuracy to solve the stitching gap problem caused by uneven illumination.

Arunachalam et al. (2018) applied the traditional techniques of RGB segmentation, edge detection and feature extraction for fruit quality control where fruits are classified as defected or fresh, based on the colors of fruit peel. Such inspection tasks are very labor-intensive and time-consuming performed by human. An AOI system is developed to minimize classification error and processing time. Tout (2018) designed a system for wheel defect detection. Cameras allocate in a hemispherical way for capturing the whole surface of a wheel from all sides. The defects for inspection include surface scratches, marks, and different geometrical deformations in shape and size. Characteristic holes of the wheel are used as registration to enhance alignment accuracy and reduce false alarm rate.

Most of the previous AOI systems developed for wide-area inspection are based on views overlapping and ROI alignment. The defects to inspect either are at a background with even intensity or well aligned for template matching. Very few of the systems are applicable for inspecting defects over a ball. Yu et al. (2021) developed an AOI system for defects on the surface of a  $\text{Si}_3\text{N}_4$  ceramic ball. The system acquires defect images using a locating device, eliminates image noises by stationary wavelet transform, and enhance image contrast using nonlinear filtering. Experiments are implemented to verify the effectiveness of their algorithm.

Golfball is a growing and popular sport. Golfball surface defects could be various in shape, size, and color. They could spread randomly over the whole surface of the ball (Asia Quality Focus). Some defects

such as dirt mark, inferiority and seam buffing flaw could appear casually on dimple surfaces along with glare light. Some defects such as logo scratch, logo protrusion/intrusion, print misalignment and incorrect print color could appear as attachment to a logo or inside it. It has a strong need to invest on AOI equipment for the economic reason.

Many successful golfball producers undergo strict inspection to ensure their highest product quality, while some choose to skip quality control to cut the cost. Strategic Automation (2021) developed many commercialized AOI machines, station by station for golfball orientation alignment, sorting, and inspection. Integro Technologies (2021) developed a deep learning system for inspection and sortation of a variety of logos printing on golfball surfaces. They implement discrete analysis tools to optimize the learning reliability and performance. An eight-station sequential operation machine can achieve an operating rate of 35 balls/min. However, their theoretical scheme and performance index such as false alarm rate are literally unknown.

The diameter of a standard golfball is about 42.75~42.95mm. Nonetheless, logo-related defects could be as small as 0.2~0.5mm in either dimension. Therefore, some golfball defects must be inspected under high image resolution and limited depth of focus. A local view is normally full of logos and/or dimple patterns under uneven illumination. Precise ROI alignment over the dimple surface is difficult. Lin (2007) studied the logo-related defect inspection problems by logo contours extraction. Mechanism for sequential control of ball orientation is designed to rotate logos into a focused view automatically. A degradation measure is proposed based on the accumulation of the turn angle of logo contours for evaluating logo quality. Experiments show that when the escape rate vanishes, the false-alarm rate is 1.23%.

Wu *et al.* (2016) designed illumination devices to reduce glare light reflective from the coating surface of golfball. Area-scan cameras are used to acquire images with good contrast for automatic defect detection. Some subtle flaws are detected with an improved false alarm rate and manpower reduction. Lin *et al.* (2020) proposed an image stitching method using optimization to achieve a whole-ball-surface (WBS) image fused from multiple views covering the whole surface of a golfball. Defect detection by WBS-to-WBS matching between test and template is proposed.

This study is devoted to developing a novel AOI system for inspecting various golfball surface defects. All defects are detected based on a template WBS image constructed offline using Lin's image stitching method (Lin *et al.*, 2020). However, we inspect defects in a view-to-view mapping basis to reduce effectively the process time.

By view-to-view mapping, we search for a best mapping for a test view, based on a reduced set of

Zernike Moments (ZMs) over a grid of template views. A similarity measure assisted with supplement is proposed to accomplish the mapping.

ZMs are traditional image descriptors used in application of image recognition (Prokop *et al.*, 1992; Shang *et al.*, 2000; Ma *et al.*, 2001; Mukundan *et al.*, 1995). ZMs are mutually independent descriptors and invariant to rotation (Teague, 1980). By this invariance property, rotation can be negligible in searching for a view-to-view mapping. In addition, we found that ZMs have good competence against additive defects. This property is useful to assure a proper mapping.

However, the invariance properties of ZMs depend heavily on the accuracy of ZMs, while traditional numerical computation of ZMs could suffer from geometric and integration errors (Liao *et al.*, 1998). In this regard, Xin *et al.* (2007) proposed a polar tiling layout of image with piecewise continue variation, and cubic spline interpolation is applied to compute ZMs with good accuracy.

In this study, we employ Xin's method for ZMs computation. Defects are classified into the groups of logo-attached and non-logo. We extract logo-related and non-logo binary images out of a test view by color thresholding. Difference between the binary images of test and template provides information for defect detection. Approach for fine-tuning of the mapping is proposed in case a better detection accuracy is required.

The rest of the paper is organized as follows. Section 2 describes the coordinate system of view, view mapping and discretization. Section 3 reviews formula for computing a reduced set of ZMs and rotation. Section 4 presents a similarity measure with supplement and experiments based on the reduced set of ZMs for view mapping. The defect inspection method proposed is discussed in Section 5. Defects to detect include logo-attached and non-logo examples. Finally, Section 6 presents the conclusions of this paper.

## VIEW MAPPING AND DISCRETIZATION

Figure 1 gives a WBS image fused from 14 local views of a whole golfball surface using Lin's image stitching with optimization (Lin *et al.*, 2020). The WBS image has two large groups of logos and one small group of logos. The resolution of the local views is 640x480 pixels; the WBS image has the resolution of 1000x500, and it comprises all views as template.

In this study, the views of template are discretized into a grid as shown in Fig. 2. The discrete inclination angles are  $N_k \varphi_s = \frac{\pi}{N_k} k$  where  $N_k$  denotes the number of intervals along the inclination axis and  $0 \leq \varphi_s \leq \pi$ . The discrete azimuthal angles are  $\theta_s = \frac{2\pi}{N_i} i$  where

$N_i$  denotes the number of intervals along the azimuthal axis and  $0 \leq \theta_s < 2\pi$ . Each point of the grid denotes a view and all views assume normal to the golfball surface.

By color thresholding, the primary colors of the WBS image are black (0x14211E), brown (0x552213), dark green (0x72A974), and light green (0x8FCF8C) where the number of pixels of each color is in an ascending order. The background renders dark and light green colors due to uneven illumination over the spherical and dimple surface, but black and brown are the colors of logos.

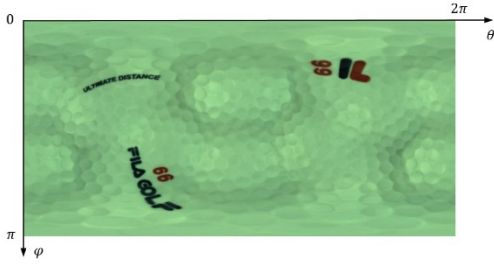


Fig. 1. Coordinate of a WBS image.

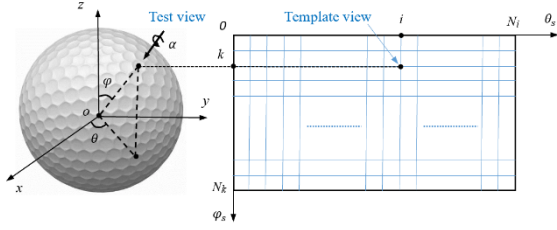


Fig. 2. Discretization of template views.

## ZERNIKE MOMENTS

For a continuous function  $f(\rho, \theta)$ , the ZMs of order  $n$  with repetition  $m$  is (Teague, 1980)

$$Z_{nm} = C_{nm} - jS_{nm} = \frac{n+1}{\pi} \int_0^{2\pi} \int_0^1 f(\rho, \theta) R_{nm}(\rho) e^{-jm\theta} \rho d\rho d\theta, \quad (1)$$

where  $j = \sqrt{-1}$ ;  $n$  is a nonnegative integer and  $m$  is an integer such that  $n - |m|$  is even and nonnegative;  $C_{nm}$  and  $S_{nm}$  denote the real and imaginary parts of  $Z_{nm}$ , respectively;  $R_{nm}(\rho)$  is the Zernike polynomial, and

$$R_{nm}(\rho) = \sum_{s=0}^{(n-|m|)/2} \frac{(-1)^s (n-s)! \rho^{n-2s}}{s! \left(\frac{n-|m|}{2}-s\right)! \left(\frac{n+|m|}{2}-s\right)!}. \quad (2)$$

In this study, we employ Xin's method for ZMs computation (Xin *et al.*, 2007). Only the centered circular image with a radius of 228 pixels of a view is used. The image is transformed to a polar tiling layout with piecewise continue variation, and cubic spline interpolation is applied. If the image rotates, the ZMs become (Bai, 2007)

$$Z_{nm}^{(\alpha)} = Z_{nm} e^{-jm\alpha}, \quad (3)$$

where  $Z_{nm}^{(\alpha)}$  denotes the ZMs after the rotational angle of  $\alpha$ , counterclockwise.

### Rotation and Phase Angle

Equation (3) leads to the rotational invariance property, and

$$\alpha = \frac{\alpha_t - \alpha_s + 2\pi}{m}, \quad n - |m| = 0, 2, 4, \dots, \quad (4)$$

where  $\alpha_s$  denotes the phase angle of ZMs of template;  $\alpha_t$  the phase angle of ZMs of test,

$$\alpha_s = \tan^{-1} \left( \frac{S_{nm}}{C_{nm}} \right), \quad \alpha_t = \tan^{-1} \left( \frac{S_{nm}^{(\alpha)}}{C_{nm}^{(\alpha)}} \right). \quad (5)$$

Without loss of generality, we assume all phase angles of template ZMs are zero (*i.e.*,  $\alpha_s = 0$ ). Then, the template ZMs of the grid is

$$Z^{(0)} = \left\{ Z_{nm}^{(0)}(i, k) \mid i = 0, 1, \dots, N_i; \quad k = 0, 1, \dots, N_k; \quad n - |m| \text{ is even} \right\}. \quad (6)$$

The phase angle  $\alpha_t$  relates with the rotational angle a test view relative to the template. We assume it is unknown in practical applications.

The magnitude of  $m$  must be greater than 0. For each ZM, we can have  $m$  tentative solutions for  $\alpha_t$  by Eq. (4). Therefore, we choose  $n$  as an odd number. The solution set of a larger  $|m|$  comprises that of a smaller  $|m|$ . We classify all solutions into  $n$  groups by nearest neighboring algorithm, and the median of the biggest group is elected as the solution for  $\alpha_t$ .

### Reduced Set of Zernike Moments

Theoretically, ZMs form a complete set of descriptors if  $n$  is infinitely large. However, use of a finite  $n$  is more practical in application. We found that by experiment a reduced set for  $n = 11$  and positive  $m$  is appropriate for view-to-view mapping.

This reduced set has 21 ZMs for each of the grid views, *i.e.*

$$Z_r^{(0)} = \left\{ Z_{11}^{(0)}(i, k), Z_{31}^{(0)}(i, k), \dots, Z_{11,9}^{(0)}(i, k), Z_{11,11}^{(0)}(i, k) \mid i = 0, 1, \dots, N_i; \quad k = 0, 1, \dots, N_k \right\}. \quad (7)$$

For a test view, the reduced set is

$$Z_r^{(\alpha_t)} = \left\{ Z_{11}^{(\alpha_t)}(\varphi_t, \theta_t), Z_{31}^{(\alpha_t)}(\varphi_t, \theta_t), \dots, Z_{11,9}^{(\alpha_t)}(\varphi_t, \theta_t), Z_{11,11}^{(\alpha_t)}(\varphi_t, \theta_t) \right\}, \quad (8)$$

where the rotational angle  $\alpha_t$  of the test view is relative to that of template. Note that the order  $n$  set to be 11 here is simply from the computational point of view.

Figure 3 shows the distributions of  $|Z_{nm}^{(0)}|$  over the grid where  $n=5$ ,  $m=1, 3, 5$ .  $|Z_{nm}^{(0)}|$  denotes the magnitude of  $Z_{nm}^{(0)}$ .  $Z_{11}^{(0)}$ ,  $|Z_{31}^{(0)}|$ , and  $|Z_{51}^{(0)}|$  have similar distribution patterns as shown in Fig. 3(a), 3(b), and 3(c), wherever logos reside, the gradient of distribution is higher. As  $m$  increases, the patterns

disperse and the magnitude of the distribution decreases as shown in Fig. 3(d), 3(e) and 3(f). It reveals that this reduced set of ZMs of different orders supplementing to each other can work as a good descriptor for a view-to-view mapping.

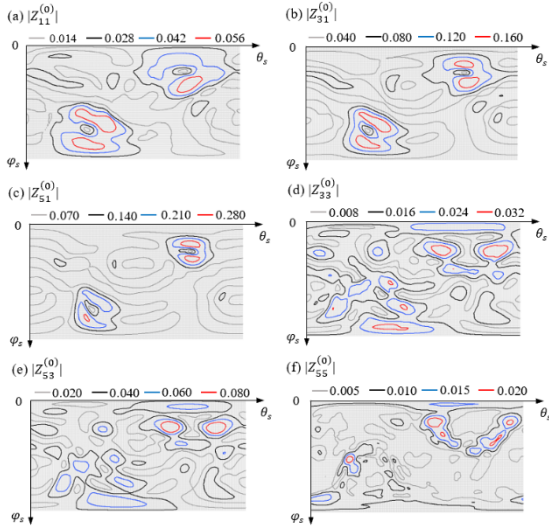


Fig. 3 Distributions of  $|Z_{nm}^{(0)}|$  over the grid for  $n=5$ ,  $m=1, 3, 5$ .

### SIMILARITY AND SUPPLEMENTAL MEASURES

In this study, a similarity measure for evaluating the similarity between test and template views is proposed:

$$\gamma(i, k) = \frac{\mathbb{C}(i, k)}{\max[\mathbb{C}(i, k)]}, i = 0, 1, \dots, N_i; k = 0, 1, \dots, N_k, \quad (9)$$

where  $\gamma(i, k)$  is the similarity measure, and  $0 \leq \gamma(i, k) \leq 1$ . It evaluates the degree of matching between a test view and the template at the point  $(i, k)$ , based on the reduced set of ZMs;  $\max[\cdot]$  denotes the maximum function;  $\mathbb{C}(i, k)$  is a counter for the template view at the point  $(i, k)$ .

It counts the number of ZMs of the reduced set of test and template satisfying the following conditions, and  $\max[\mathbb{C}(i, k)] = 21$  according to Eq. (7):

$$(1 - \varepsilon_l) \min[\mathbb{N}_{nm}(i, k)] \leq |Z_{nm}^{(\alpha_t)}(\varphi_t, \theta_t)| \leq (1 + \varepsilon_u) \max[\mathbb{N}_{nm}(i, k)], \quad (10)$$

where  $\min[\cdot]$  denotes the minimum function;  $\varepsilon_l$  and  $\varepsilon_u$  are extension tolerances in concern of the geometric and integration errors in computing ZMs, and  $\varepsilon_l = \varepsilon_u = 0.01$  are set in this study;  $\mathbb{N}_{nm}(i, k)$  is a set of the 4 neighbors of  $|Z_{nm}^{(0)}(i, k)|$ , i.e.

$$\mathbb{N}_{nm}(i, k) = \{|Z_{nm}^{(0)}(i - 1, k)|, |Z_{nm}^{(0)}(i + 1, k)|, |Z_{nm}^{(0)}(i, k - 1)|, |Z_{nm}^{(0)}(i, k + 1)|\}. \quad (11)$$

We acknowledge a view mapping from

$Z_{nm}^{(\alpha_t)}(\varphi_t, \theta_t)$  to  $Z_{nm}^{(0)}(i, k)$  is constructed wherever the similarity measure satisfies

$$\gamma_l < \gamma(i, k) \leq \gamma_u, i = 0, 1, \dots, N_i; k = 0, 1, \dots, N_k, \quad (12)$$

where  $\gamma_l$  and  $\gamma_u$  denote the lower and upper bounds of similarity between two views, respectively.

The proposed view mapping is dynamic by setting the bounds varying to avoid possible null mapping. For example, we may set initially  $(\gamma_l, \gamma_u) = (0.9, 1.0)$ , and then reduce both the bounds by 0.1 simultaneously until Eq. (12) is satisfied. The consequence of mapping also depends on the size of the interval  $[\gamma_l, \gamma_u]$ . A small interval size may sustain in a null mapping, while a large one will lead to one-to-many mappings where Eq. (12) is satisfied.

### Color Difference Measure

In case of one-to-many mappings, we will choose  $\tau$  mappings ( $\tau \geq 1$ ) of highest similarity measures as tentative for searching by a supplemental color difference measure. This supplemental measure is based on average of the absolute difference of RGB components between the primary colors of test and template in priority.

By priority, a primary color should play a more dominant role in measure of view matching if it is less in population in the views. Therefore, we establish priorities for each of the primary colors of the WBS image to assist the proposed supplemental measure.

In this study, the priority for each of the primary colors, from high to low, is black, brown, dark and light green. Our supplemental measure starts with the color of the highest priority by checking the average of absolute difference of RGB components between two views. If the color of a higher priority is absent, the color of next priority substitutes. The tentative of the smallest average of absolute difference is acknowledged as the best mapping.

### Experimental Examples

In this study, the mapping of views is discretized into a grid of 720x360 points. The total time required to compute the set of  $Z_r^{(0)}$  is about 36 hours using the software of LabVIEW 2020 executing on a laptop equipped with Intel(R) Core(TM) i7-8750H CPU @ 2.20GHz, 16.0 GB RAM, and x64-based processor.

The mappings for 1,000 random views is shown in Fig. 4(a) where the center of a circle indicates a test view. The radius of the circle indicates accumulation of mappings ( $N_m$ ) for the test view. A bigger circle denotes more mappings which occur especially at the views near the North Pole ( $\varphi = 0$ ) or South Pole ( $\varphi = \pi$ ) where the contents of views are much alike.

Figure 4(b) shows accumulation of views ( $N_v$ ) vs. accumulation of mappings. The proposed dynamic bounds setting guarantees no null mapping, but 95% of mapping are one-to-many, and only 5% are one-to-one mapping.

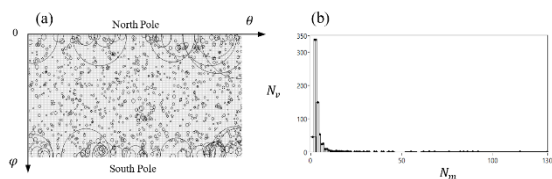


Fig. 4 Mapping results of 1,000 random views (a) center of circle indicating a view, radius of circle indicating accumulation of mappings (b) accumulation of views vs. accumulation of mappings.

For one-to-one mapping, the only mapping itself is the best mapping. For one-to-many mappings, we temporarily choose the one with the highest similarity measure as the best mapping (*i.e.*,  $\tau = 1$ ). Under the best mapping, errors of inclination, azimuthal, and rotational angles are shown respectively in Fig. 5 (a), 5(b), and 5(c) where the radii of the circles indicate the magnitudes of error.

In Fig. 5(a), the mean and maximal inclination angle errors are 0.004 and 0.017, respectively. The maximum occurs at the view shown in Fig. 6(a) where  $(\varphi_t, \theta_t, \alpha_t) = (2.269, 0.889, 5.659)$ . The mapping view of template without rotation is  $(\varphi_s, \theta_s) = (2.286, 0.881)$  as shown in Fig. 6(b). The relative rotational angle computed using Eq. (4) is  $\alpha_s = 5.656$ . With rotation, the mapping view is shown in Fig. 6(c). Shown in Fig. 6(d) in red pixel is the misalignment of logos between test and template with azimuthal and rotational errors as small as 0.008 and 0.003, respectively.

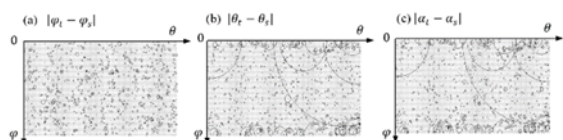


Fig. 5 Magnitude of mapping errors (a)  $|\varphi_t - \varphi_s|$ : max = 0.017, mean = 0.004 (b)  $|\theta_t - \theta_s|$ : max = 1.133, mean = 0.012 (c)  $|\alpha_t - \alpha_s|$ : max = 1.132, mean = 0.013.

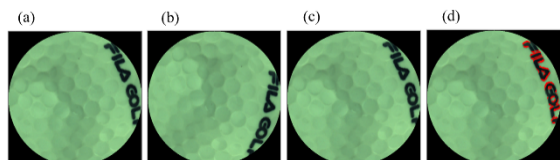


Fig. 6 Mapping views of the maximal inclination angle error in Fig. 5(a) for  $\tau = 1$ , (a) test view:  $(\varphi_t, \theta_t, \alpha_t) = (2.269, 0.889, 5.659)$ , (b) best mapping without rotation:  $(\varphi_s, \theta_s) = (2.286, 0.881)$ , (c) best mapping with rotation:  $(\varphi_s, \theta_s, \alpha_s) = (2.286, 0.881, 5.656)$ , (d) misalignment of logos between test and template.

The misalignment of Fig. 6(d) can be improved based on a best mapping chosen from tentative using the proposed supplemental measure. For  $\tau = 2$ , improvement of the misalignment is significant as shown in Fig. 7(c), despite that change of the mapping angles is less than 1.1% as shown in Fig. 7(a) and 7(b).

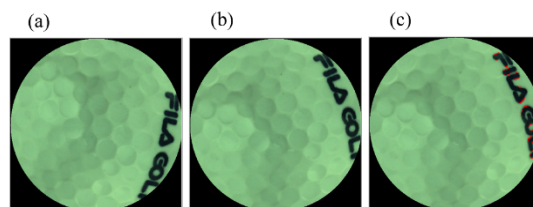


Fig. 7 Mapping views of the maximal inclination angle error in Fig. 5(a) for  $\tau = 2$ , (a) best mapping without rotation:  $(\varphi_s, \theta_s) = (2.260, 0.890)$ , (b) best mapping with rotation:  $(\varphi_s, \theta_s, \alpha_s) = (2.260, 0.890, 5.659)$ , (c) misalignment of logos between test and template.

In Fig. 5(b), the mean and maximal azimuthal angle errors are 0.012 and 1.133, respectively. The maximum occurs at the view shown in Fig. 8(a) where  $(\varphi_t, \theta_t, \alpha_t) = (0.002, 5.526, 1.088)$ . The mapping view of template without rotation is  $(\varphi_s, \theta_s) = (0.000, 0.375)$  as shown in Fig. 8(b). Since the test view is very close to the North Pole, the azimuthal and rotational angles of the view correlate to each other strongly. The logos of the two views align to each other well despite the substantial errors of azimuthal and rotational angles whose sums differ only by 0.001 between test and template. The two views perfectly match with each other as shown in Fig. 8(c) where the inclination angle error is only 0.002. Therefore, the errors of azimuthal and rotational angles will be combined for evaluation, hereafter.

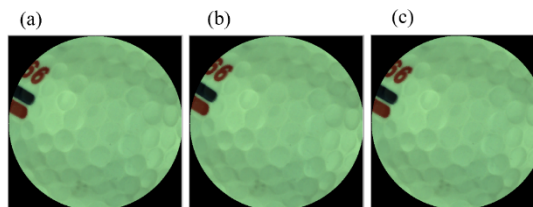


Fig. 8 Mapping views of the maximal azimuthal angle error in Fig. 5(b) for  $\tau = 1$ , (a) test view:  $(\varphi_t, \theta_t, \alpha_t) = (0.002, 5.526, 1.088)$ , (b) best mapping without rotation:  $(\varphi_s, \theta_s) = (0.000, 0.375)$ , (c) best mapping with rotation:  $(\varphi_s, \theta_s, \alpha_s) = (0.000, 0.375, 6.240)$ .

## DEFECT INSPECTION

In this study, the defects to detect are classified into logo-attached and non-logo. The former may include logo protrusion/intrusion, scratch, print misalignment, and incorrect print color, while the latter may include surface dirt mark, inferiority, and seam buffing flaw.

### Classification of Image Blobs

Each pixel of a test view is classified into a primary color by minimizing the sum of square of RGB component differences between the pixel and the primary colors, *i.e.*

$$F_t(x, y) = \kappa, x = 1, \dots, N_x, y = 1, \dots, N_y, \quad (13)$$

where  $F_t(x, y)$  is a color classified function of test view;  $N_x$  and  $N_y$  the dimensions of the test view along the x- and y-axis, respectively, and  $N_x = 640$ ,  $N_y = 480$ , and  $\sqrt{x^2 + y^2} \leq 228$  in this study;  $\kappa$  is an integer of 1 to 4 representing the color of black, brown, dark green, or light green, respectively according to the following criteria:

$$\min_{\kappa=1, \dots, N_c} \{ [f_{tR}(x, y) - p_{\kappa R}]^2 + [f_{tG}(x, y) - p_{\kappa G}]^2 + [f_{tB}(x, y) - p_{\kappa B}]^2 \}, \quad (14)$$

where  $N_c$  denotes the number of the primary colors, and  $N_c = 4$  in this study;  $f_{tR}$ ,  $f_{tG}$ , and  $f_{tB}$  are the RGB components of a test pixel;  $p_{\kappa R}$ ,  $p_{\kappa G}$ , and  $p_{\kappa B}$  are the RGB components of a primary color.

### Classification and Difference of Images

In this study, black and brown are the colors of logos. Therefore, we extract a logo-related binary image out of the test view using Eqs (13) and (14), *i.e.*,

$$\Phi_t(x, y) = \begin{cases} 1, & \text{if } F_t(x, y) = 1 \text{ or } 2 \\ 0, & \text{if } F_t(x, y) = 3 \text{ or } 4 \end{cases} \quad (15)$$

where  $\Phi_t(x, y)$  denotes the logo-related binary image.

Besides, a non-logo binary image is defined below:

$$\Psi_t(x, y) = \overline{\Phi_t(x, y)} \cdot \Gamma_t(x, y), \quad (16)$$

$$\Gamma_t(x, y) = \Gamma_{tR}(x, y) + \Gamma_{tG}(x, y) + \Gamma_{tB}(x, y), \quad (17)$$

$$\Gamma_{tR}(x, y) = \begin{cases} 1, & \text{if } |f_{tR}(x, y) - p_{\kappa R}| \geq \delta \\ 0, & \text{otherwise} \end{cases}, \quad (18)$$

$$\Gamma_{tG}(x, y) = \begin{cases} 1, & \text{if } |f_{tG}(x, y) - p_{\kappa G}| \geq \delta \\ 0, & \text{otherwise} \end{cases}, \quad (19)$$

$$\Gamma_{tB}(x, y) = \begin{cases} 1, & \text{if } |f_{tB}(x, y) - p_{\kappa B}| \geq \delta \\ 0, & \text{otherwise} \end{cases}, \quad (20)$$

where  $\Psi_t(x, y)$  denotes the non-logo binary image; “ $\cdot$ ” denotes the AND operator, “ $\overline{\quad}$ ” the NOT operator, “ $+$ ” the OR operator;  $\delta$  is a threshold of color difference, and  $\delta = 40$  is set in this study;  $\Gamma_{tR}(x, y)$ ,  $\Gamma_{tG}(x, y)$ ,  $\Gamma_{tB}(x, y)$  are binary images of test view  $f_t(x, y)$  with one of RGB components different from that of a primary color, respectively by thresholding;  $\Gamma_t(x, y)$  is a union binary image of  $\Gamma_{tR}(x, y)$ ,  $\Gamma_{tG}(x, y)$ , and  $\Gamma_{tB}(x, y)$ .

The logo-related binary image may provide information of logo protrusion/intrusion, scratch and surface dirt mark falsely classified as logo-related comparing with the logo related binary image of a

template view. The non-logo binary image may provide information of logo print misalignment, incorrect print color, inferiority, seam buffing flaw after comparing with the non-logo binary image of a template view. However, color gradient across the border of a logo is normally high under normal illumination where false non-logo binary images may arise. Such false binary images require removal in this study.

In this study, the differences between the logo-related and non-logo binary images of test and template are defined as

$$\Delta\Phi(x, y) = \Phi_t(x, y) \times \Phi_s(x, y), \quad (21)$$

$$\Delta\Psi(x, y) = \Psi_t(x, y) \times \Psi_s(x, y), \quad (22)$$

where  $\Delta\Phi$  and  $\Delta\Psi$  denote the difference of the binary images of logo-related and non-logo between test and sample; “ $\times$ ” is the EXCLUSIVE-OR operator;  $\Phi_s$  and  $\Psi_s$  are logo-related and non-logo binary image of template with rotation.

### Fine-tuned Mapping and False Alarm Rate

The misalignment of logos in Fig. 7(c) is primarily due to the inclination angle error of 0.009 while the grid of mapping has the resolution of 0.00873. Further improvement of the alignment accuracy by fine-tuning is proposed.

The proposed fine tune is based on searching for local minimization of the sum of the image values of  $\Delta\Phi$  by adjusting the inclination, azimuthal, and rotational angles of view, sequentially in a small step size, *i.e.*

$$\min_{\alpha_s \pm q\Delta\alpha_s} \min_{\theta_s \pm q\Delta\theta_s} \min_{\varphi_s \pm q\Delta\varphi_s} \sum[\Delta\Phi], q = 0, 1, \dots, \quad (23)$$

where  $\sum[\Delta\Phi]$  denotes the sum of the image values of  $\Delta\Phi$ ;  $\Delta\varphi_s$ ,  $\Delta\theta_s$ ,  $\Delta\alpha_s$  denote the step size for fine-tuning along an associated axis, respectively.

After fine-tuning, a blob image of  $\Delta\Phi$  is classified as logo-attached if the Euclidian distance between a blob pixel and a pixel of the contours of  $\Phi_s$  is less than a threshold of distance, *i.e.*

$$|\mathcal{B}_{\Delta\Phi}(x, y) - \mathcal{C}_{\Phi_s}(x, y)| < \lambda, \quad (24)$$

where  $\mathcal{C}_{\Phi_s}$  denotes the contours of  $\Phi_s$ ;  $\mathcal{B}_{\Delta\Phi}$  the blob images of  $\Delta\Phi$ ;  $\lambda$  the threshold of distance for logo attachment detection, and it is set  $\lambda = 9$  by experiment in this study.

For a blob image of  $\mathcal{B}_{\Delta\Phi}$  attached to logo, the width of the blob image along a contour of  $\mathcal{C}_{\Phi_s}$  is defined as below:

$$w = \max_{\forall(x, y) \in \mathcal{C}_{\Phi_s}} \min_{\forall(x', y') \in \Delta\Phi} |\mathcal{B}_{\Delta\Phi}(x', y') - \mathcal{C}_{\Phi_s}(x, y)|, \quad (25)$$

where  $w$  denotes the width of the blob image along a contour of  $\mathcal{C}_{\Phi_s}(x, y)$ .

By thresholding, we acknowledge a blob image of  $\mathcal{B}_{\Delta\Phi}$  as a logo-attached defect if

$$w > \omega, \quad (26)$$

where  $\omega$  denotes a threshold of width.

A small threshold of width determines the sensitivity of detection to miniature logo-attached

defects. However, the false alarm rate ( $\epsilon$ ) could be high when logo misalignments mean. Inspection of 1,000 random views without defects is accomplished, and the results are shown in Fig. 9. The black lines in the figures denote the distributions of accumulation of views of true positive vs. errors of mapping inclination and combination of azimuth-and-rotation where the width of lines is 0.00017 for accumulation. The red circles in the figures denote the distributions of false alarm (false positive) vs. the errors of mapping.

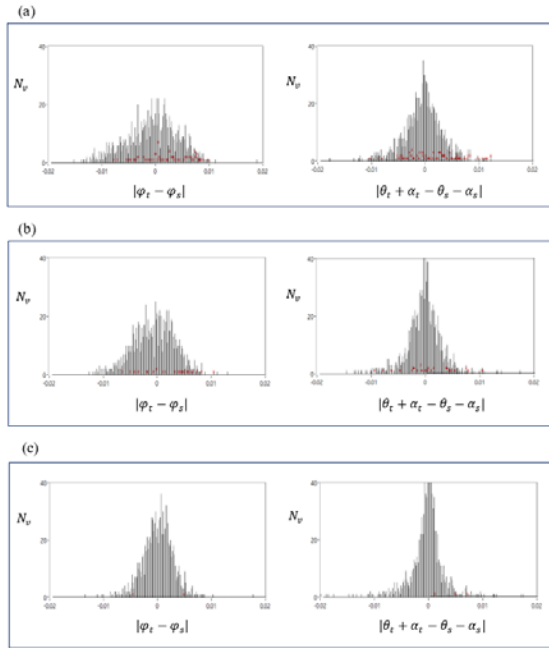


Fig. 9 Distributions of true/false positives vs. mapping errors for 1,000 random views (a)  $\tau=1$ ,  $\epsilon=16.2\%$  (b)  $\tau=2$ ,  $\epsilon=5.6\%$  (c)  $\tau=2$ ,  $\Delta\varphi_s=\Delta\theta_s=\Delta\alpha_s=0.25$ ,  $\epsilon=0.6\%$ .

For  $\tau=1$ , the distributions without fine-tuning are shown in Fig. 9(a) where  $\epsilon=16.2\%$ . For  $\tau=2$ , the distributions without fine-tuning are gathering toward the center. The variance of the distribution reduces as shown in Fig. 9(b) where  $\epsilon=5.6\%$ . The accuracy of view-to-view mapping is improved. By fine-tuning where  $\Delta\varphi_s = \Delta\theta_s = \Delta\alpha_s = 0.25$ , we execute the sequential searching of Eq. (23) twice for minimization. The mapping accuracy is further improved as shown in Fig. 9(c) where  $\epsilon=0.6\%$ .

### Experimental Examples

Defects are added to views by labor as shown in Fig. 10, to demonstrate the robustness of the proposed view mapping against defect disturbances. The added defects are small, dashed logo protrusion/intrusion, thin-cracked logo protrusion/intrusion, and surface dirt marks as shown at the left of Figs 10(a)~10(d).

Logo misalignment and surface dirt are marked in

red at the right of Figs 10(a)~10(d) where  $\tau=3$  and  $\omega=3$  are set without fine-tuning. For protrusion/intrusion defects, precise logo alignment and successful defect detection are achieved. Despite the dirt marks added may disturb alignment as shown in Fig. 10(c), this disturbance is minor and does not affect dirt marks detection by using the proposed non-logo binary image.

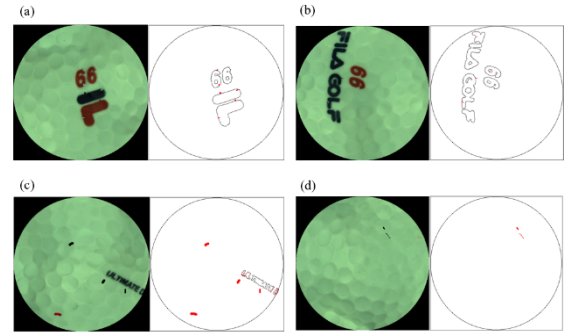


Fig. 10 Proficiency of the proposed inspection algorithm against small-added defects (a) dashed protrusion/intrusion (b) thin-cracked protrusion/intrusion (c) spot marks (d) dash marks.

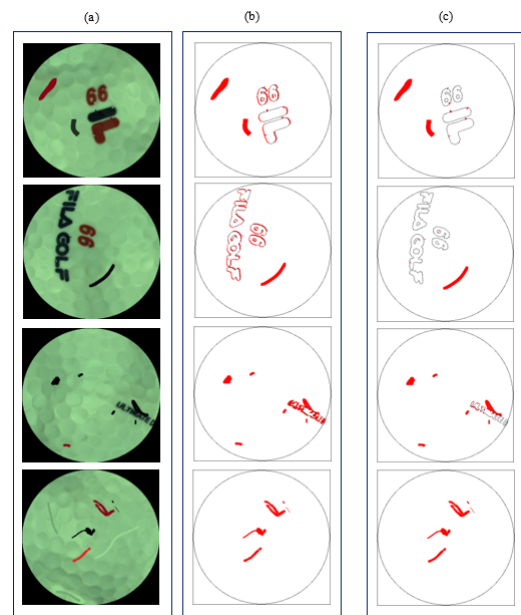


Fig. 11 Demonstration of the proposed inspection algorithm for assembly defects (a) test views with assembly defects (b) detection without fine-tuning (c) detection with fine-tuning.

Continue the previous examples with more defects added as shown in Fig. 11(a). All added defects are assemblies of different shapes, sizes, and colors. With the above parameter settings and no fine-tuning, the robustness of the proposed view mapping against

disturbances still hold, despite logo misalignment is now somehow noticeable as shown in Fig. 11(b). These assemblies of disturbance do not affect dirt marks detection by using the proposed non-logo binary image. Note that the “surface dirt mark defects” of dark and light green colors are added for test on purpose. It illustrates that the proposed non-logo defect detection using the binary images  $\Delta\Psi$  can solve the problem of uneven illumination by using a proper threshold of color difference where  $\delta=40$  is set in this study.

With fine-tuning and  $\Delta\varphi_s = \Delta\theta_s = \Delta\alpha_s = 0.25$ , the alignment accuracy is significantly improved as shown in Fig. 11(c). Dashed and thin-cracked protrusion/intrusion are isolated and detectable.

## CONCLUSIONS

This study is devoted to developing a novel approach for surface defect inspection of golfball. We propose a view-to-view mapping algorithm based on a reduced set of ZMs where the order of the reduced set is open to option. It is set in this study simply to shorten the computational time. The proposed mapping algorithm has good ability against additive defects as shown in Fig. 11. This ability is essential and explains why the proposed defect inspection approach can be successful to apply.

The mapping is from test to a template view defined by  $N_{nm}(i, k)$  in Eq. (11), which is the 4 neighbors of the view. This adjacent region definition makes the mapping have better robustness against the geometric and integration errors of ZMs. Other definition of  $N_{nm}(i, k)$  to improve further the robustness performance is feasible.

The proposed inspection algorithm can be implemented in a single view in a sequential operation to reduce the inspection time. All the experiments conducted in this study are based on 1,000 random test views, using the software of LabVIEW 2020 running on a desktop equipped Intel(R) Core(TM) i7-8750H CPU @ 2.20GHz, 16.0 GB RAM, and x64-based processor. The average cycle time of our view-to-view inspection is about 2.0 seconds. This is very competitive to the deep learning system developed by Integro Technologies, Inc..

The false alarm rate achieved in this study is as low as 0.6% as shown in Fig. 9(c). In addition, the proposed inspection algorithm is equipped with a non-logo detector by color thresholding, which gives a flexible parameter  $\delta$  for design for overcoming the uneven illumination problem. The algorithm with fine-tuning can detect simultaneously logo-attached and non-logo defects of assemblies of different shapes, sizes, and colors in a single view and resolution. To our best knowledge, these performance indexes of related studies are unknown in the literal domain.

The idea of the proposed view-to-view mapping is applicable for defect inspection on a wide highly-

curved/plane surface or other ball surface where precise ROI alignment is difficult to perform on line or in a short time.

## REFERENCES

- Arunachalam, S., Kshatriya, H. H., and Meena, M., “Identification of Defects in Fruits Using Digital Image Processing,” *International Journal of Computer Sciences and Engineering*, Vol. 6, Issue 10, pp. 637-640 (2018).
- Asia Quality Focus, Sports balls inspection process. <https://www.intouch-quality.com/blog/sports-balls-inspection-process-quality-control> (2021).
- Bai, X. F., “Application of the improved Zernike moment in cultural relic image retrieval,” *Computer Applications and Software*, Vol. 24, No. 3, pp. 135-136 (2007).
- Huang, M., Ma, Y. and Gong, Q-P, “Image Recognition Using Modified Zernike Moments,” *Sensors & Transducers*, Vol. 166, Issue 3, pp. 219-223 (2014).
- Integro Technologies Corp, Golf ball sortation and inspection, North Carolina, USA. <https://www.integro-tech.com/> (2021).
- Kim, Y. S. and Kim, W. Y., “Content-based trademark retrieval system using a visually salient feature,” *Image Vis. Comput.*, Vol. 16, pp. 931–939 (1998).
- Kuo, S. and Cross, G. R., “A two-step string-matching procedure,” *Pattern Recogn.* Vol. 247, pp. 711–716 (1991).
- Liao, S. X. and Pawlak, M., “On the accuracy of Zernike moments for image analysis,” *IEEE Trans. Pattern Anal. Mach. Intell.*, Vol. 20, No. 12, pp. 1358–1364 (1998).
- Lin, K-C, “Study of Automatic Optical Inspection for Golf Logo Quality”, *J. Electron. Imaging*, Vol. 16, No. 3, 033016 (2007).
- Lin, K-C and Hu, F-W, “A Multi-View Image Capture Machine Design and Image Fusion Processing for Golf Ball Surface Inspection,” *Journal of the Chinese Society of Mechanical Engineers*, Vol. 41, Issue 4, pp.417-425 (2020).
- Ma, Z. M., Zhang, G. and Yan, L., “Shape feature descriptor using modified Zernike moments,” *Pattern Analysis and Applications*, Vol. 14, Issue 1, pp. 9-22 (2011).
- Mukundan, R. and Ramakrishnan, K. R., “Fast computation of Legendre and Zernike moments,” *Pattern Recognition*, Vol. 28, Issue 9, pp. 1433–1442 (1995).
- Peng, H-L and Chen, S-Y, “Trademark shape recognition using closed contours,” *Pattern Recogn. Lett.* Vol. 18, pp. 791–803 (1997).
- Prokop, R. J. and Reeves, A. P., “A survey of moment based techniques for unoccluded object

- representation,” Graph. Models Image Process—CVGIP, Vol. 54, Issue 5, pp. 438–460 (1992).
- Rosati, G., Boschetti, G., Biondi, A., and Rossi, A., “Real-time defect detection on highly reflective curved surfaces,” Optics Lasers Eng. Vol. 47, pp. 379–384 (2009).
- Shang, L-Q and Du, Y-J, “Application in image recognition based on Hu moment and Zernike moments,” Journal of Xi’an Institute of Technology, Vol. 20, Issue 1, pp. 53-56 (2000).
- Strategic Automation, Automatic golfball inspection machine, Sentry-1, Massachusetts, USA. <https://strategic-automation.com/> (2021).
- Teague, M. R., “Image analysis via the general theory of moments,” J. Opt. Soc. Am., Vol. 70, Issue 8, pp. 920–930 (1980).
- Tout, K., “Automatic Vision System for Surface Inspection and Monitoring: Application to Wheel Inspection,” HAL Id: tel-01801803, <https://tel.archives-ouvertes.fr/tel-01801803> (2018).
- Wu, H-H, Su, J-W, and Chen, C-L, “Automatic Optical Inspection System Design for Golf Ball,” Proc. SPIE 9971, Applications of Digital Image Processing XXXIX, 99712S (2016).
- Xin, Y-Q, Pawlak, M. and Liao, S., “Accurate computation of Zernike moments in polar coordinates,” IEEE Trans Image Process, Vol.16, Issue 2, pp.581-587 (2007).
- Yu, D-L, Zhang, H-L, Zhang, Xi-H, Liao, D-H, and Wu N-X, “Si3N4 Ceramic Ball Surface Defects’ Detection Based on SWT and Nonlinear Enhancement,” Hindawi, Math. Prob. in Eng., Vol. 2021, Article ID 4922315, 9 pages, <https://doi.org/10.1155/2021/4922315> (2021).

## NOMENCLATURE

$\varphi$	inclination angle	$Z_r^{(0)}$	reduced set of ZMs of template
$\varphi_s$	inclination angle of template view	$Z_r^{(\alpha_t)}$	reduced set of ZMs of test
$\varphi_t$	inclination angle of test view	$\gamma$	similarity measure
$N_k$	number of grid intervals along inclination axis	$\mathbb{C}$	counter for template view
$\theta$	azimuthal angle	$\varepsilon_l$	extension tolerances
$\theta_s$	azimuthal angle of template view	$\varepsilon_u$	extension tolerances
$\theta_t$	azimuthal angle of test view	$\mathbb{N}$	set of 4 neighbors
$N_i$	number of grid intervals along azimuthal axis	$\gamma_l$	lower bound of similarity
$Z_{nm}$	Zernike moment of order $n$ with repetition $m$	$\gamma_u$	upper bound of similarity
$C_{nm}$	the real part of $Z_{nm}$	$\tau$	number of mappings
$S_{nm}$	the imaginary part of $Z_{nm}$	$N_v$	accumulation of views
$R_{nm}$	Zernike polynomial of order $n$ with repetition $m$	$N_m$	accumulation of mappings
$\alpha$	rotational angle	$F_t$	color classified function of test view
$\alpha_s$	phase angle of ZMs of template	$N_x$	dimension of test view along x-axis
$\alpha_t$	phase angle of ZMs of test	$N_y$	dimension of test view along y-axis
		$\kappa$	index integer of a primary color
		$N_c$	number of primary colors
		$f_t$	binary image of test view
		$f_{tR}$	$R$ component of a test pixel
		$f_{tG}$	$G$ component of a test pixel
		$f_{tB}$	$B$ component of a test pixel
		$p_{\kappa R}$	$R$ component of a primary color
		$p_{\kappa G}$	$G$ component of a primary color
		$p_{\kappa B}$	$B$ component of a primary color
		$\Phi_t$	logo-related binary image of test view
		$\Phi_s$	logo-related binary image of template view
		$\Delta\Phi$	difference of logo-related binary image between test and sample
		$\Delta\varphi_s$	step size of fine-tuning along inclination axis
		$\Delta\theta_s$	step size of fine-tuning along azimuthal axis
		$\Delta\alpha_s$	step size of fine-tuning along rotational axis
		$\sum$	sum of image values
		$\Psi_t$	non-logo binary image of test view
		$\Psi_s$	non-logo binary image of template view
		$\Delta\Psi$	difference of non-logo binary image between test and sample
		$\delta$	threshold of color difference
		$\Gamma_t$	union binary image of $\Gamma_{tR}$ , $\Gamma_{tG}$ , and $\Gamma_{tB}$
		$\Gamma_{tR}$	see definition in Eq. (18)
		$\Gamma_{tG}$	see definition in Eq. (19)
		$\Gamma_{tB}$	see definition in Eq. (20)
		$\mathcal{C}_{\Phi_s}$	contours of $\Phi_s$
		$\mathcal{B}_{\Delta\Phi}$	blob images of $\Delta\Phi$
		$\lambda$	threshold of distance
		$w$	width of blob image along contour of $\mathcal{C}_{\Phi_s}$
		$\omega$	threshold of width
		$\epsilon$	false alarm rate

# 藉由影像對映及Zernike矩 之高爾夫全球表面瑕疵檢 測法

林毅欽 馬敏雄

崑山科技大學機械工程系暨研究所

## 摘要

本研究提一高爾夫全球表面瑕疵檢測新法，本法採用測試影像之Zernike矩次集合與二維陣列樣板影像，尋找出兩者間之最佳對映，進而實踐樣板影像比對及瑕疵檢測。依據 1,000 次隨機影像測試實驗顯示，本實驗完成每顆高爾夫球表面瑕疵檢測，所需平均電腦計算時間約為 2 秒，本檢測速度與一般商業化深度學習系統約略相當。然而，本檢測法具精密的影像對映微調機制，可獲得低至 0.6%之錯誤警報率。依作者的瞭解，目前並無可參考文獻提出更低之錯誤警報率。本檢測結合有色彩分割技法，可克服非均勻照明下易造成瑕疵誤判的問題。線上檢測時，本法僅須擷取單一解析測試影像，即可同時針對不同形狀、尺寸及顏色商標及非商標之混合瑕疵作檢出。本影像對映法特別適用於其他大範圍平面或曲面、不易執行精確特徵對位或無法短時間內完成有效線上瑕疵檢測之應用。